PCCP

RSC Publishing

PAPER

View Article Online
View Journal | View Issue

Cite this: *Phys. Chem. Chem. Phys.*, 2013, **15**, 3304

An advanced cathode for Na-ion batteries with high rate and excellent structural stability†

Dae Hoe Lee,‡ Jing Xu‡ and Ying Shirley Meng*

Received 11th December 2012,
Accepted 20th December 2012

DOI: 10.1039/c2cp44467d

www.rsc.org/pccp

Layered P2-$Na_x[Ni_{1/3}Mn_{2/3}]O_2$ ($0 < x < 2/3$) is investigated as a cathode material for Na-ion batteries. A combination of first principles computation, electrochemical and synchrotron characterizations is conducted to elucidate the working mechanism for the improved electrochemical properties. The reversible phase transformation from P2 to O2 is observed. New configurations of Na-ions and vacancy are found at $x = 1/3$ and 1/2, which correspond to the intermediate phases upon the electrochemical cycling process. The mobility of Na-ions is investigated using the galvanostatic intermittent titration technique (GITT) and the Na diffusion barriers are calculated by the Nudged Elastic Band (NEB) method. Both techniques prove that the mobility of Na-ions is faster than Li-ions in the O3 structure within the $1/3 < x < 2/3$ concentration region. Excellent cycling properties and high rate capability can be obtained by limiting the oxygen framework shift during P2–O2 phase transformation, suggesting that this material can be a strong candidate as a sustainable low-cost Na-ion battery cathode.

Introduction

The worldwide demand to develop electrical energy storage is growing as renewable energy technologies such as wind and solar energy conversion become increasingly prevalent. Going forward with large-scale stationary electrical storage, new battery systems which are more reliable and lower in cost will be required.[1] Li-ion batteries have been considered one of the most suitable candidates; however there are concerns about the cost and the geopolitical limit of lithium sources. In order to develop the alternative energy storage devices, usage of abundant and environmental-friendly elements is needed. Ambient temperature sodium-based batteries have the potential for meeting those requirements due to the wide availability and low cost. In addition, they provide an alternative to Li-ion batteries, since the gravimetric energy density is comparable to Li-ion batteries.

Studies on electrochemical insertion and extraction of Na-ions began in the late 1970s and the early 1980s.[2–6] Due to the tremendous success of Li-ion batteries, limited efforts have been spent on Na-ion batteries during the past two decades. More intensive research studies on various cathode materials have been conducted since the 2000s with the concern regarding the long term viability of Li chemistry. A series of studies on layered cathode materials for Na-ion batteries have been conducted. Sodium-based layered cathode materials are categorized into two major groups which are P2 and O3 type. The first letter "P" or "O" refers to the nature of the site occupied by an alkali ion (prismatic or octahedral), and "2" or "3" refers to the number of alkali layers in the repeat unit perpendicular to the layering.[7] The P2-Na_xCoO_2 material has been investigated by Delmas's group to reveal the phase transformations and electrochemical behavior.[8–11] Layered O3 type Na_xVO_2,[12] Na_xCrO_2,[13] Na_xMnO_2,[14] and Na_xFeO_2[15] have also been reported to be able to host Na-ions upon charge and discharge, however the capacity fading was significant. A study by Lu and Dahn demonstrated that the P2-layered oxide, $Na_{2/3}[Ni_{1/3}Mn_{2/3}]O_2$, can reversibly exchange Na-ions in sodium cells.[16,17] In addition to the layered materials, some phosphates based on either the olivine[18–21] or NASICON[22–24] structures appeared to hold particular promise. The strong inductive effect of the PO_4^{3-} polyanion that moderates the energetics of the transition metal (TM) redox couple generates relatively high operating potentials in Na-ion batteries. More recently, advanced Na compounds with novel structures have been prepared and characterized. Li substituted $Na_{1.0}Li_{0.2}Ni_{0.25}Mn_{0.75}O_2$ was studied by Kim *et al.* and displayed 95 mAh g^{-1} of specific capacity, excellent cycling and rate capabilities. It is hypothesized that Li in the TM layer improves the structural stability during the cycling.[25] The research on single crystal $Na_4Mn_9O_{18}$ nanowires was conducted by Cao *et al.*, and they demonstrated that their Na-ion

Department of NanoEngineering, University of California San Diego, La Jolla, CA 92037, USA. E-mail: shirleymeng@ucsd.edu

† Electronic supplementary information (ESI) available. See DOI: 10.1039/c2cp44467d

‡ These two authors contributed equally.

battery exhibited 110 mAh g^{-1} and good cycling properties until 100 cycles.[26] This compound has drawn significant attention due to the large tunnels in the structure, which are suitable for incorporation of Na-ions.[27,28] However, they still require the substitution of inactive species or nano-scale fabrication which might diminish the advantage of using low cost sodium. As we mentioned earlier, the reversibility of P2-$Na_{2/3}[Ni_{1/3}Mn_{2/3}]O_2$ has been demonstrated experimentally. However no subsequent studies have been conducted for nearly a decade presumably due to the poor electrochemical performances, though the material is lower in cost and easy to synthesize. Since the Na-ion is 70% larger in volume than the Li-ion, unique and robust structures are required for long-term stability and new intermediate phases due to Na-ion vacancy ordering may be expected during the cycling. Such unique crystal structural phenomena and related electronic properties can be efficiently investigated using first principles computational techniques because of their atomistic level precision.[29] Despite the many advantages, only a few computational studies on the physical or chemical properties of Na-ion batteries have been performed.[30,31]

In this work, we combine both experimental and computational methods to investigate the structural, electronic, and electrochemical properties of P2-$Na_{2/3}[Ni_{1/3}Mn_{2/3}]O_2$. The phase transformations upon the charge and discharge were precisely characterized by synchrotron XRD and confirmed by first principles calculations. New intriguing patterns of Na-ion vacancy orderings were identified, which correspond to the intermediate phases during electrochemical cycling. The diffusion barriers calculated by the nudged elastic band (NEB) method and experimentally measured by the galvanostatic intermittent titration technique (GITT) demonstrate that the mobility of Na-ions is indeed faster than that of Li-ions in a typical O3 structure. High rate capability and excellent cycling properties can be obtained by limiting the P2–O2 phase transformation.

Results and discussion

Fig. 1a shows the experimental voltage profiles as a function of the specific capacity in the voltage range from 2.3–4.5 V at a low rate that represents near-equilibrium (C/100). The as-calculated voltage profiles (dotted line) match qualitatively well with the experimental voltage pattern. The theoretical capacity of P2-$Na_{2/3}[Ni_{1/3}Mn_{2/3}]O_2$ is 173 mAh g^{-1} considering the Ni^{2+}–Ni^{4+} redox reaction which is associated with 2/3 of Na-ions. However the material exhibits 190 mAh g^{-1} of specific capacity at the 1st charge which is 17 mAh g^{-1} higher than the theoretical value presumably due to possible electrolyte decomposition above 4.4 V. Reversibly, 140 mAh g^{-1} of specific capacity was obtained at the following discharge, indicating that the reversibility is around 74%. It was observed that there are two major intermediate phases at 3.5 and 4.0 V upon the charge, which correspond to the Na content of 1/2 and 1/3, respectively. The dQ/dV profiles presented in Fig. S1 (ESI†) give us more accurate observation on the intermediate phases. A long plateau was observed at 4.22 V indicating that a two phase reaction is occurring. According to the energy calculation

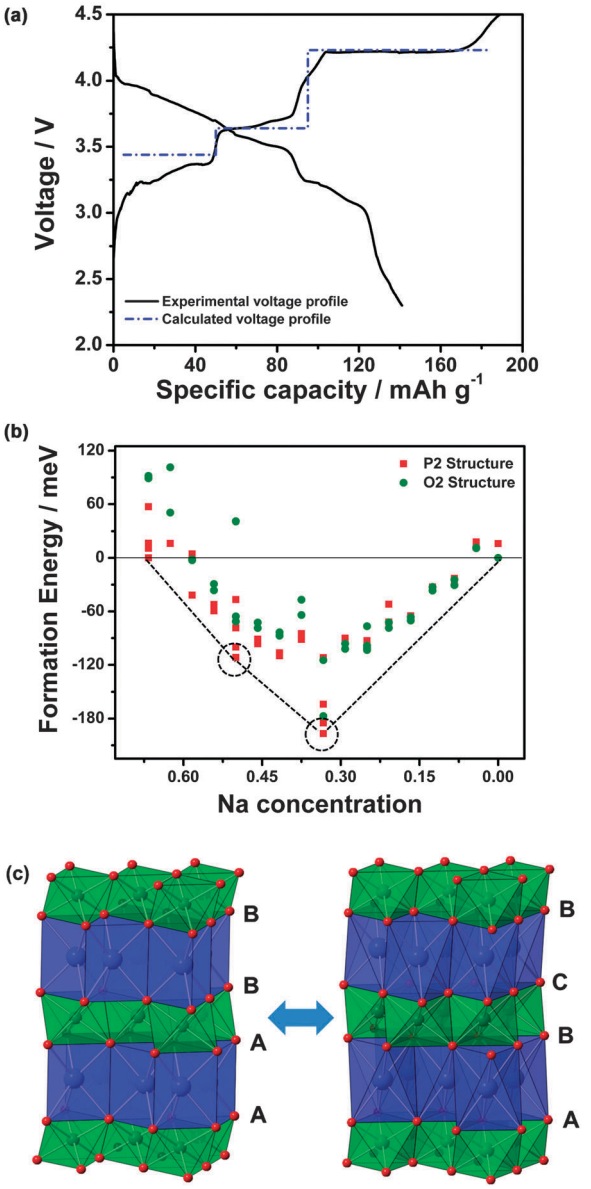

Fig. 1 (a) Electrochemical profiles for Na/$Na_{2/3}[Ni_{1/3}Mn_{2/3}]O_2$ cells between 2.3 to 4.5 V at C/100 current rate including the calculated voltage profiles (dotted line), (b) calculated formation energies at different Na concentration including the convex hull (dotted line), and (c) structural schematics of P2 and O2 including the stacking sequence of oxygen layers.

shown in Fig. 1b, P2 has the lowest energy in the region $1/3 < x < 2/3$, thus it is the most stable phase. After removing all Na-ions ($x = 0$), O2 is the more stable phase whose energy is 25 meV f.u.$^{-1}$ (1 f.u. contains one $[Ni_{1/3}Mn_{2/3}]$ unit) lower than the P2 phase. This energy difference is significant as the DFT accuracy is about 3 meV f.u.$^{-1}$. The schematics of P2 and O2 structures are shown in Fig. 1c, where Na-ions are coordinated by the prismatic site and octahedral site. Therefore the oxygen stacking sequences of P2 and O2 are "AABB" and "ABCB" respectively. It is easy to visualize that the O2 structure can be formed by simply gliding of two oxygen layers without breaking the bonds between oxygen and TMs. The coexistence of these

two phases leads to the long plateau at 4.22 V in the region $0 < x < 1/3$. Using P2 at $x = 2/3$ and O2 at $x = 0$ as the reference states, the convex hull connecting all the lowest formation energies (dotted line in Fig. 1b) is constructed, which has been extensively used as a direct measure of phase stability.[32,33] The two points (dotted circle in Fig. 1b) at $x = 1/2$ and $1/3$ shown on the convex hull correspond to two new stable intermediate phases. In order to identify the intermediate phases, synchrotron XRD and advanced calculation are applied.

As shown in Fig. 2a, *ex situ* synchrotron XRD was taken at the different Na contents to investigate the new phases and the precise sodium intercalation and de-intercalation mechanisms. All the reflections can be indexed in the hexagonal system using the *P*63/*mmc* space group except for the fully charged phase. The peaks at 3.4° and 6.7° are associated with the hydrated P2 phase.[34] As reported in earlier work, it was observed that the phase transformation from P2 to O2 occurs above 4.2 V upon the charge, and the P2 phase is reversibly regenerated at the following discharge to 3.75 V. Although the voltage rises were clearly observed at 3.5 V and 4.0 V, no obvious changes are detected in the XRD peak positions and intensities, which are consistent with the earlier report. On the pristine and fully discharged XRD patterns, the small peaks were detected at 7.23°, 7.54° and 7.8° possibly due to the existence of Na-ion vacancy superstructure ordering (Fig. 2a right), which will be discussed later. In order to obtain precise information regarding the structural changes, Rietveld refinement was carried out to identify the site occupancies and lattice parameters. Detailed Rietveld refinement fitting results of $Na_x[Ni_{1/3}Mn_{2/3}]O_2$ are shown in Table S1 (ESI†). Changes in lattice parameters are shown in Fig. 2b.

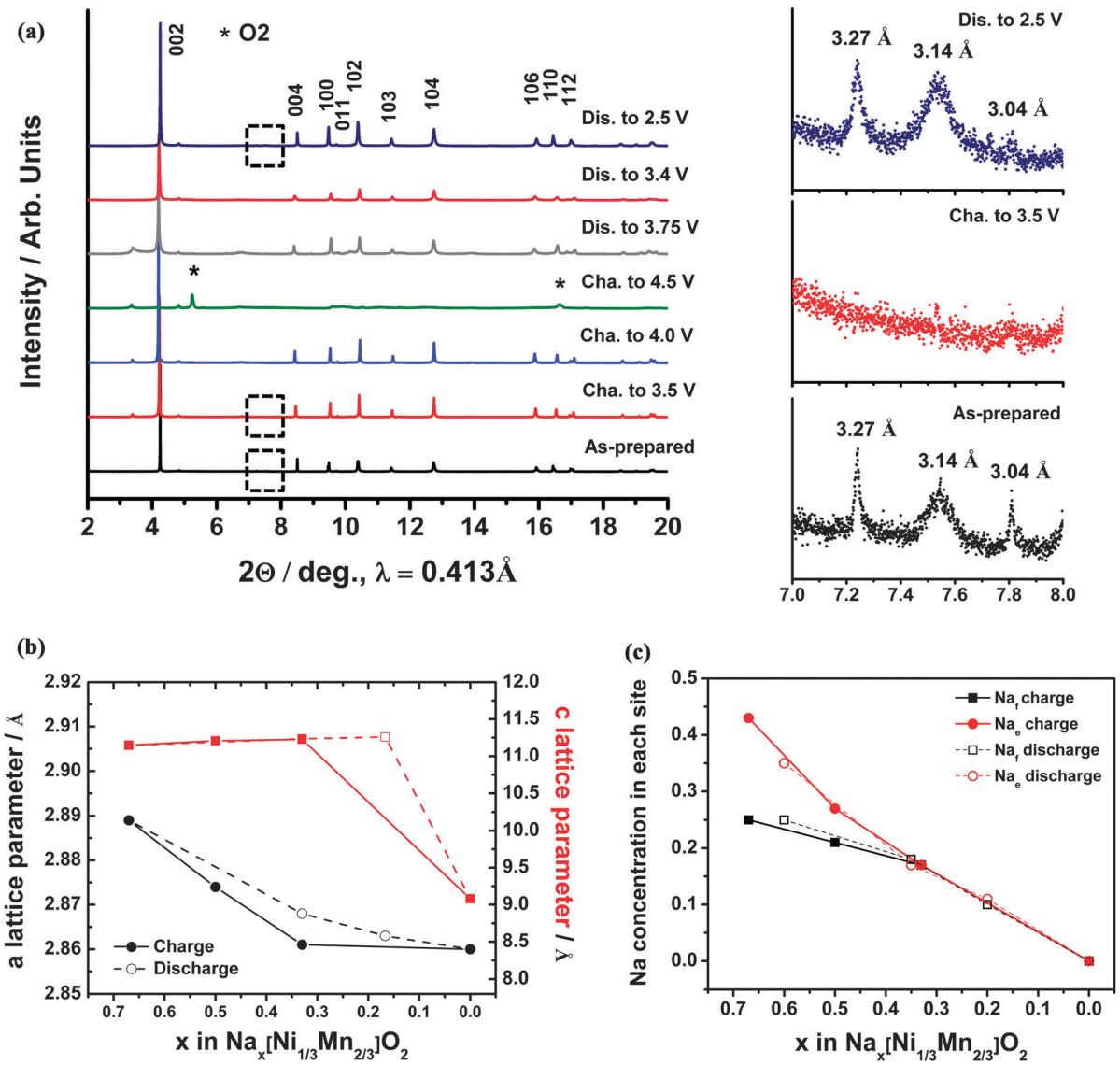

Fig. 2 (a) Synchrotron X-ray diffraction patterns of $Na_x[Ni_{1/3}Mn_{2/3}]O_2$ at different *x* concentrations during the 1st cycle and (right) enlarged XRD patterns of pristine, charged to 3.5 V and fully discharged electrodes between 7° to 8° including *d*-spacing, (b) changes in *a* and *c* lattice parameters, and (c) changes in Na_f and Na_e site occupancies upon the 1st cycle.

During Na-ion extraction, the *a* lattice parameter, which is dominated by the M–M distance, decreases slightly as expected from the oxidation of Ni ions. The *a* lattice parameter is maintained after 1/3 Na-ions are extracted from the structure possibly due to the P2 to O2 phase transformation. However, the *c* lattice parameter slowly increases until *x* approaches to 1/3 and then decreases drastically at the P2 to O2 transformation region, where *x* is lower than 1/3. Once 1/3 of the Na-ions are extracted, successive O layers directly face each other without any screening effect by Na-ions. Therefore, the increased electrostatic repulsion between these oxygen layers expands the *c* lattice parameter along the *z*-axis. After 1/3 Na-ions are removed from the structure, oxygen layers prefer to shift resulting in O2 stacking. Though the changes in the *c* lattice are relatively large, P2–O2 transformation requires no bond breaking between oxygen and TM indicating that the required energy is low and the possibility of structural collapse is small. The changes in the lattice parameters appear to be reversible at the following discharge. The changes in the site occupancies of Na-ions during the 1st charge and discharge are shown in Fig. 2c. There are two different Na sites in the P2 structure, which are face sharing with MO_6 (Na_f) and edge sharing (Na_e).[35] The total refined Na amount in the as-prepared sample is 0.68, where 0.25 of Na are sitting on the Na_f site and 0.43 of Na are located in the Na_e site. In general, the simultaneous occupancy of both sites allows the in-plane Na^+–Na^+ electrostatic repulsion to be minimized leading to globally stable configurations. However, the Na_e site is energetically more favorable in comparison with the Na_f site due to lower electrostatic repulsion between Na^+ and TM^+. Upon the charge, the Na-ions in the Na_e site appear to extract slightly faster than Na-ions in the Na_f site until *x* approaches to 1/3, possibly due to the higher in-plane Na^+–Na^+ electrostatic repulsion in the Na_e site. However, the occupancies in both sites are uniformly extracted after that concentration. Upon the discharge, Na-ions in both sites are uniformly filled until *x* approaches to 1/3, where $Na_f = Na_e = 0.17$. Although the simultaneous occupancies of both sites are essential to minimize the in-plane electrostatic repulsion, it appears that this repulsion is saturated once around 0.17 Na-ions are filled in each site. After this saturation, the electrostatic repulsion between Na^+ and TM^+ energetically governs the occupancies leading to the majority of Na-ions in the Na_e site.

As discussed above, the overall occupancy ratio is decided by the competition between sites energy and electrostatic repulsion. This competition also has effects on the in-plane arrangement of Na-ions. Our calculation reveals that the other two short voltage steps at 3.5 V and 4.0 V mainly result from the in-plane ordering effect. In Fig. 3a, the stable ordering patterns in pristine materials consist of Na_f connecting in a very intriguing pattern. The distance between such Na_f ions is $2a_{hex}$, which has been named "large zigzag" (LZZ) by Meng *et al.*[36,37] The other simpler ordered states where all Na atoms form a "honeycomb", "diamond" or "row"[38–40] with no Na_f sites occupied, have at least 20 meV f.u.$^{-1}$ higher energy compared to that of LZZ. Therefore the ground state ordering has part of the Na-ions in high energy sites (Na_f) in order to achieve the stability by minimizing the electrostatic repulsion among Na-ions. In fact, the LZZ pattern has also been detected by our synchrotron XRD. As illustrated in Fig. 2a right, three superstructure peaks in a pristine electrode are observed, which correspond to the d-spacing of around 3.2 Å. This value is consistent with the average distance between nearest neighbor Na-ions in the proposed LZZ pattern. Superstructure peaks disappear as Na-ions are extracted and the concentration deviates from 2/3, however they are recovered in the fully discharged electrode, suggesting that such Na-ion vacancy ordering is preferred at $x = 2/3$ concentration. Though there is a possibility that the TM charge ordering could exist, XRD cannot probe the charge ordering as the TM-ions have similar scattering intensities. Therefore, the superstructure observed is surely from Na-ion vacancy ordering. At $x = 1/2$ (Fig. 3b), the ordering is changed from LZZ to rows, where one row of Na_f and two rows of Na_e arrange in the plane alternatively. When the concentration is reduced to 1/3, Na orders in rows on either Na_e or Na_f sites in a single layer (Fig. 3c). However, the stacking faults along the *c*-axis caused by the P2 to O2 oxygen framework shift prevent us from finding peaks related to superstructures

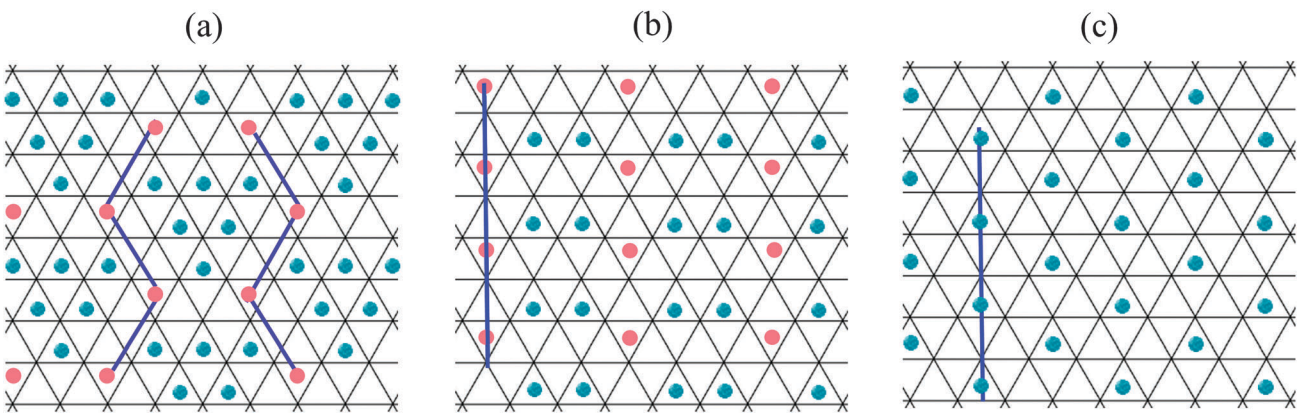

Fig. 3 In-plane Na-ions orderings of $Na_x[Ni_{1/3}Mn_{2/3}]O_2$ in the triangular lattice (a) $x = 2/3$, (b) $x = 1/2$, and (c) $x = 1/3$ (blue balls: Na-ions on Na_e sites, pink balls: Na-ions on Na_f sites).

by the power diffraction.[41] A more detailed study to shed light on the evolution of these superstructures upon cycling is currently underway. This is the first time that Na-ion ordering effects are reported and discussed in $Na_x[Ni_{1/2}Mn_{2/3}]O_2$, though a lot of work has been done on Na_xCoO_2, a thermoelectric oxide material.[36,37] Based on our calculation, this ordering preference is essential during the electrochemical cycling and common for all Na compounds.

Noticing that Na-ions prefer different in-plane orderings at different Na concentrations, it is hypothesized that such a fast self-arrangement must require high Na-ions mobility in the material. A NEB calculation is applied to further study the activation barrier in the $Na_x[Ni_{1/2}Mn_{2/3}]O_2$. The Na-ions diffusion paths of P2 (left) and O2 (right) are shown in Fig. 4a. The path with the minimum energy in P2 structure is passing through a shared face between two neighboured Na prismatic sites. For O2 structure, the Na-ions have to cross the tetrahedron between two octahedral sites by means of a divacancy mechanism.[42] According to Fig. 4b, Na-ions need only around 170 meV to be activated in the diffusion process, when the concentration range is $1/3 < x < 2/3$; this activation barrier is lower than half of its corresponding O3–Li compounds.[43] In the P2–O2 phase transformation region, the required energy increases to over 290 meV, indicating a low hopping rate and slow Na-ion mobility. This big energy difference results from the distinct diffusion paths. It is evident that in P2 structure, the diffusion path of Na-ions is more spacious than that in the O2 structure leading to a much lower activation barrier. Once most of the Na-ions are removed, the energy barrier decreases back to 250 meV due to the relatively small repulsion from neighboring ions in the dilute concentration. In addition to the NEB calculation, GITT was performed to measure the Na-ions mobility as a function of Na concentration in $Na_x[Ni_{1/3}Mn_{2/3}]O_2$, since it is known to be more reliable to calculate the chemical diffusion coefficient, especially when intrinsic kinetics of phase transformations are involved.[44] Fig. 4c shows the variation of a chemical diffusion coefficient of Na-ions (D_{Na}) in $Na_x[Ni_{1/3}Mn_{2/3}]O_2$ determined from the GITT profiles. The D_{Na} is calculated using the eqn S1 (ESI†) and GITT profiles are shown in Fig. S3 (ESI†). The minimum value of D_{Na} is observed in $0 < x < 1/3$, where P2 to O2 phase transformation occurs. However, the D_{Na} in the solid solution region ($1/3 < x < 2/3$) exhibits 7×10^{-9}– 1×10^{-10} cm^2 s^{-1}, which is around 1 order of magnitude higher than the corresponding Li diffusivity in O3 compounds, where D_{Li} is 3×10^{-9}– 2×10^{-11} cm^2 s^{-1}.[45] Both NEB calculation and GITT demonstrated that Na-ion diffusion in P2-$Na_{2/3}[Ni_{1/3}Mn_{2/3}]O_2$ is fast.

To obtain the information on the oxidation states of TM, the density of states (DOS) of Ni and Mn 3d orbitals in $Na_x[Ni_{1/2}Mn_{2/3}]O_2$ (x = 2/3, 1/3, 0) are calculated and presented in Fig. 5. Since the Ni and Mn ions sit in the octahedral site surrounded by 6 oxygen ions, 3d bands of TM ions split into t_{2g} and e_g bands. In the Ni DOS for pristine materials (x = 2/3, black curve in Fig. 5a), the energy levels of both spin-up and

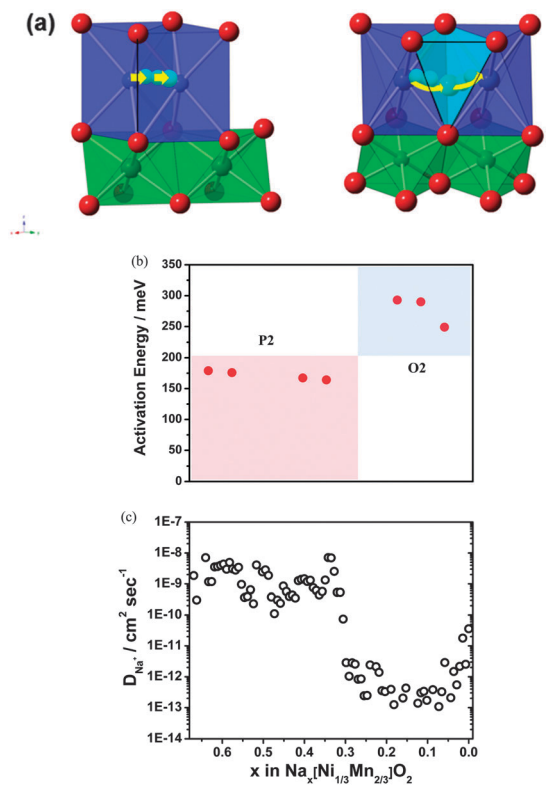

Fig. 4 (a) The diffusion paths of P2 (left) and O2 (right), (b) calculated activation energy using the NEB method, and (c) chemical diffusion coefficient of Na-ions (D_{Na}) in $Na_x[Ni_{1/3}Mn_{2/3}]O_2$ calculated from GITT as a function of the Na concentration.

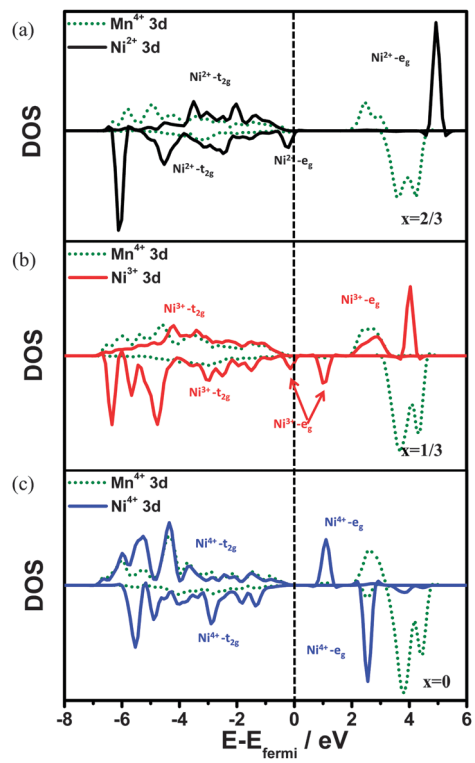

Fig. 5 The electronic structures of Ni 3d and Mn 3d orbitals in $Na_x[Ni_{1/3}Mn_{2/3}]O_2$ at (a) x = 2/3, (b) x = 1/3, and (c) x = 0.

spin-down states in the t_{2g} orbitals are lower than the Fermi energy, indicating that the t_{2g} orbitals are fully occupied. Similarly, the spin-down states of the e_g orbitals are also full of electrons, since their energy levels are below the Fermi level. However, the energy levels of spin-up states in the e_g orbitals are above the Fermi level, indicating no orbitals are occupied. This electron configuration, $t_{2g}^6e_g^2$, by Ni DOS demonstrates the presence of Ni^{2+} in the pristine material. In the half de-intercalated state (x = 1/3, red curve in Fig. 5b), the Ni DOS suggests that the t_{2g} orbitals are still completely occupied. However the spin-down states of e_g orbitals are separated into two peaks, where one peak has lower energy than the Fermi level. This indicates that one of the spin-down e_g orbitals is occupied leading to the $t_{2g}^6e_g^1$ electron configuration, so the existence of Ni^{3+} is confirmed at x = 1/3. After removing all Na-ions (x = 0, blue curve in Fig. 5c), most of the electrons in the e_g orbitals are removed as the energy levels of e_g orbitals are higher than the Fermi level. However, the DOS suggested that a certain amount of the electron density is still found in e_g orbitals. Based on our calculation, Ni-ions are oxidized to +3.5 at the end of the charge. On the other hand, Mn-ions remain predominately at tetravalent with fully occupied t_{2g} orbitals and completely empty e_g orbitals, independent of the changes in Na concentrations (green curve in Fig. 5a–c). In summary, our calculation illustrates the evolution of electronic structures in TM: when Na-ions are gradually extracted, Ni-ions undergo the transition of Ni^{2+}–Ni^{3+}–$Ni^{3.5+}$, while Mn-ions stay at +4 valence state upon the whole cycling maintaining the structural stability in the absence of Jahn–Teller active Mn^{3+}.

In addition to the changes in TM states, our calculation also suggests that O-ions are involved in the redox reaction providing additional electrons at the end of a charging process to keep the charge balance in the compound (Fig. 6). The valence of O-ions is investigated qualitatively from the changes of spin distribution on the O layer. In Fig. 6a, part of the O layers of the $Na_x[Ni_{1/3}Mn_{2/3}]O_2$ supercell is represented by the red balls along with the adjacent TM slab. The corresponding spin densities in the pristine and fully charged materials are shown in Fig. 6b and c, respectively. Though the plane is cut through the O layer, the spin density of Ni and Mn-ions can still be observed partially. In the pristine material (x = 2/3, Fig. 6b), well bonded O 2p electrons can be clearly observed, however, the shape of O 2p electron clouds changes significantly in the fully charged phase (x = 0), suggesting the obvious changes in O valence. Compared with the dramatic changes around O, the electron densities of Mn-ions are slightly increased due to the charge re-hybridization around O. The above results demonstrate that the extra electrons, which cannot be provided by Ni redox couples, come from O-ions during the charging stage. Similar phenomena have also been proposed in some Li compounds.[46,47] Such phenomena are likely to be attributed to the low rate and poor cycling capability at extremely low Na concentration. Detailed study to reveal the evolution of atomic and electronic structures of the TM upon cycling by *in situ* XAS is currently in progress.

The electrochemical properties of P2-$Na_{2/3}[Ni_{1/3}Mn_{2/3}]O_2$ are shown in Fig. 7. Cycling tests were carried out using different cut-off voltages (4.5 V and 4.1 V), as well as different C-rates, C/100, C/20 and C/5. The cycling performances are significantly affected by the P2–O2 phase transformation above 4.2 V. As shown in Fig. 7a, the voltage cut-off at 4.1 V prevents the P2–O2 phase transformation avoiding the dramatic changes in oxygen framework of the host structure. The 1st discharge capacity was 134 mAh g^{-1} if the cut-off voltage is 4.5 V, however the capacity retention at the 2nd discharge was 89%, and only 64% of capacity can be obtained after 10 cycles. However, the cycling excluding the phase transformation region shows excellent capacity retentions at both C/20 and C/5. The capacity at the 1st discharge was 87.8 mAh g^{-1} at C/20, which is corresponding to the insertion of 1/3 Na-ions. 94.9% of capacity can be retained after the 50th cycle at the average voltage of 3.4 V *vs.* Na^+/Na. In C/5 cycling, the 1st discharge capacity was 81.85 mAh g^{-1}, corresponding to 93% of capacity obtained at C/20. The capacity retention after the 50th cycle was 92% and

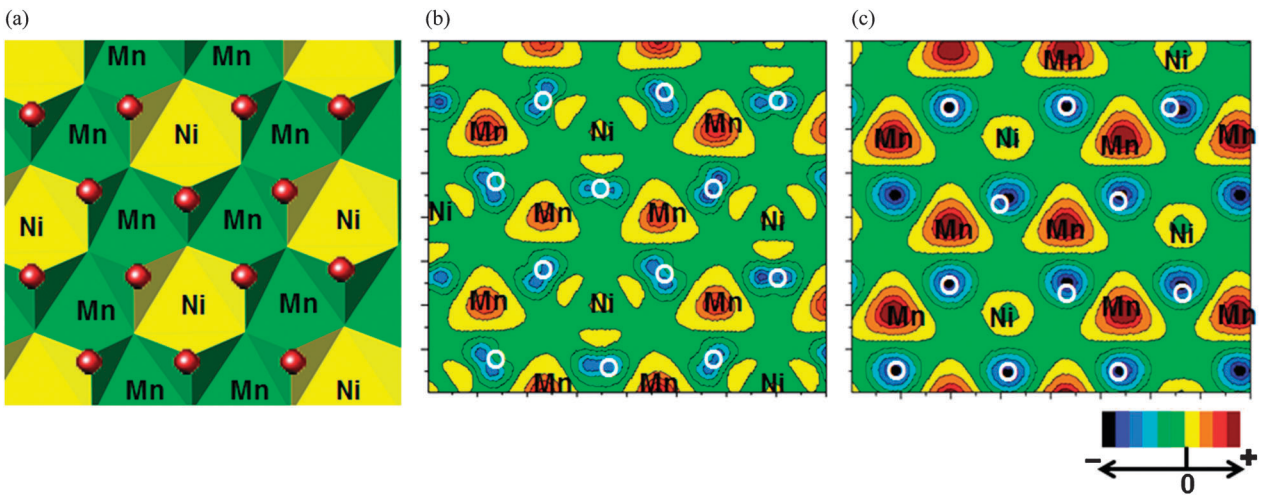

Fig. 6 (a) Schematic illustration of the oxygen layer, (b) calculated spin density cutting from an oxygen layer at x = 2/3, and (c) x = 0.

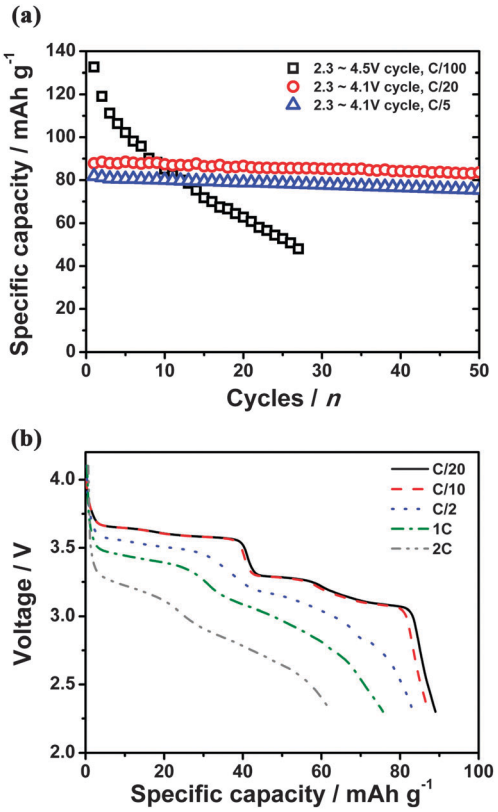

Fig. 7 The electrochemical properties of $Na/Na_{2/3}[Ni_{1/3}Mn_{2/3}]O_2$ cells, (a) cycling performances at different voltage ranges (2.3–4.1 V and 2.3–4.5 V) and different C-rates (C/100, C/20 and C/5), and (b) rate capability at C/20, C/10, C/2, 1C and 2C between 2.3–4.1 V.

the coulombic efficiency reached higher than 96% during the 50 cycles. The coulombic inefficiency in C/5 cycling is partially attributed to the side reaction between the electrolyte and the Na metal anode, and Na plating upon the charge. Since no battery grade Na metal is commercially available, our Na anode contains a certain amount of impurities. Nonetheless, the cathode still shows excellent capacity retentions during the cycling. The rate capability is also significantly improved when excluding the phase transformation region (Fig. 7b). The electrode delivered 89.0 mAh g^{-1} at C/20, 83.3 mAh g^{-1} at C/2, 75.7 mAh g^{-1} at 1C, corresponding to 85% of the capacity at C/20 and 62.4 mAh g^{-1} at 2C, 70% of the capacity at C/20. Based on the electrochemical performances, it has been demonstrated that the P2-$Na_{2/3}[Ni_{1/3}Mn_{2/3}]O_2$ material in Na-ion batteries exhibits excellent cycling stability and rate capability which are comparable to Li-ion batteries. Improvement on capacity beyond 100 mAh g^{-1} in P2 structure is possible with different TM ratios and alkali metal substitution.

Experimental

Synthesis

A co-precipitation technique was utilized for the synthesis of the materials which was previously described.[48] TM nitrates, $Ni(NO_3)_2{\cdot}6H_2O$ (99%, Acros Organics) and $Mn(NO_3)_2{\cdot}4H_2O$ (98%, Acros Organics), were titrated into a stoichiometric NaOH (Sigma-Aldrich) solution at 10 ml h^{-1} rate. The co-precipitated $M(OH)_2$ were then filtered using a centrifuge and washed three times with deionized water. The dried TM precursors were ground with a stoichiometric amount of Na_2CO_3 (anhydrous, 99.5%, Strem chemicals). The calcinations were performed at 500 °C for 5 h and at 900 °C for 14 h in air.

Electrochemistry

Cathode electrodes were prepared by mixing $Na_{2/3}[Ni_{1/3}Mn_{2/3}]O_2$ with 10 wt% acetylene black (Strem chemicals) and 5 wt% polytetrafluoroethylene (PTFE). Na metal (Sigma-Aldrich) was used as the counter electrode. 1 M $NaPF_6$ (99%, Strem chemicals) in the battery grade 67 vol% diethylene carbonate (DEC) and 33 vol% ethylene carbonate (EC) (Novolyte) were used as the electrolyte and the glass fiber GF/D (Whatman) was used as the separator. The swagelok type cells were assembled in an argon filled glove box (H_2O < 0.1 ppm) and tested on an Arbin battery cycler in the galvanostatic mode. To measure the chemical diffusion coefficient, the galvanostatic intermittent titration technique (GITT) was employed at a pulse of 17 μA (C/100) for 1 h and with 2 h relaxation time between each pulse.

X-ray diffraction

The samples for XRD were obtained by disassembling cycled batteries in an argon-filled glovebox. The cathode was washed by battery grade dimethyl carbonate (DMC) 3 times and dried in the vacuum oven at 100 °C for 24 h. The cathode film was sliced into thin pieces and mounted in the hermitically sealed capillary tubes for *ex situ* XRD. Powder diffractions of all samples were taken using synchrotron XRD at the Advanced Photon Source (APS) at Argonne National Laboratory (ANL) on beamline 11-BM (λ = 0.413384 Å). The beamline uses a sagittal focused X-ray beam with a high precision diffractometer circle and perfect Si(111) crystal analyzer detection for high sensitivity and resolution. XRD patterns were analyzed by the Rietveld refinement method using FullProf software.[49]

Computational methods

The first principles calculations were performed in the spin-polarized GGA+U approximations to the Density Functional Theory (DFT). Core electron states were represented by the projector augmented-wave method[50] as implemented in the Vienna *ab initio* simulation package (VASP).[51–53] The Perdew–Burke–Ernzerhof exchange–correlation[54] and a plane wave representation for the wave function with a cutoff energy of 450 eV were used. The Brillouin zone was sampled with a dense *k*-point mesh by Gamma packing. The supercell is composed of twenty-four formula units of $Na_{2/3}[Ni_{1/3}Mn_{2/3}]O_2$. In the supercell, there are two layers of TM, and two layers of Na-ions. The in-plane dimension is $2\sqrt{3}a_{hex} \times 2\sqrt{3}a_{hex}$. The lattice shows a *P*63/*mmc* layered structure. The atomic positions and cell parameters are fully relaxed to obtain total energy and optimized cell structure. To obtain the accurate electronic structures, a static self-consistent calculation is run, followed by a non-self-consistent calculation

using the calculated charge densities from the first step. The cell volume is fixed with internal relaxation of the ions in the second step calculation. The Hubbard *U* correction was introduced to describe the effect of localized d electrons of TM ions. Each TM ion has a unique effective *U* value applied in the rotationally invariant GGA+U approach. The applied effective *U* value given to Mn ions is 4 eV and to Ni ions is 6.1 eV, consistent with earlier work.[55–57] The migration barriers of the Na-ion and vacancy in the material are calculated using the NEB method as implemented in VASP.

Conclusions

In summary, ambient temperature Na-ion batteries have the potential to meet the requirements for large-scale stationary energy storage sources as well as an alternative to Li-ion batteries due to the natural abundance and low cost of sodium. We prepared P2-$Na_{2/3}[Ni_{1/3}Mn_{2/3}]O_2$ with excellent cycling property and high rate capability as a cathode material for Na-ion batteries. The phase transformation from P2 to O2 at 4.22 V was investigated by first principles formation energy calculation and confirmed by synchrotron XRD. The specific Na-ion orderings were found at Na = 1/3 and 1/2, which are corresponding to the voltage steps in the charging profile. Based on both GITT measurement and NEB calculation, the diffusivity of Na-ions in the P2 structure is indeed higher than that in the corresponding O3 structured Li compounds. The electronic structures have been studied and DOS calculation suggested that oxygen partially participates in the redox reaction at the end of the electrochemical charge. Consequently, it was demonstrated that the capacity retention of 95% after 50 cycles could be obtained by excluding the P2–O2 phase transformation and 85% of the reversible capacity could be retained at a 1C rate. In addition, a simple synthesis method can be used to prepare this material without any special nanoscale fabrication. Our study demonstrates that P2-$Na_{2/3}[Ni_{1/3}Mn_{2/3}]O_2$ is a strong candidate for a cathode in Na-ion batteries for large-scale energy storage.

Acknowledgements

The authors acknowledge support from the National Science Foundation under Award Number 1057170. The synchrotron X-ray diffraction patterns were collected at Argonne National Laboratory on beamline 11-BM through the general user proposal mail-in program. J. Xu acknowledges Dr S. Curtarolo and coworkers for providing the aconvasp code. This computation work used the Extreme Science and Engineering Discovery Environment (XSEDE), which is supported by National Science Foundation grant number OCI-1053575.

Notes and references

1 Z. G. Yang, J. L. Zhang, M. C. W. Kintner-Meyer, X. C. Lu, D. W. Choi, J. P. Lemmon and J. Liu, *Chem. Rev.*, 2011, **111**, 3577–3613.
2 M. S. Whittingham, *Prog. Solid State Chem.*, 1978, **12**, 41–99.
3 A. S. Nagelberg and W. L. Worrell, *J. Solid State Chem.*, 1979, **29**, 345–354.
4 C. Delmas, J. J. Braconnier, C. Fouassier and P. Hagenmuller, *Solid State Ionics*, 1981, **3–4**, 165–169.
5 J. Molenda, C. Delmas and P. Hagenmuller, *Solid State Ionics*, 1983, **9–10**, 431–435.
6 J. M. Tarascon and G. W. Hull, *Solid State Ionics*, 1986, **22**, 85–96.
7 C. Delmas, C. Fouassier and P. Hagenmuller, *Physica B and C*, 1980, **99**, 81–85.
8 F. Tournadre, L. Croguennec, I. Saadoune, D. Carlier, Y. Shao-Horn, P. Willmann and C. Delmas, *J. Solid State Chem.*, 2004, **177**, 2790–2802.
9 M. Pollet, M. Blangero, J. P. Doumerc, R. Decourt, D. Carlier, C. Denage and C. Delmas, *Inorg. Chem.*, 2009, **48**, 9671–9683.
10 D. Carlier, M. Blangero, M. Menetrier, M. Pollet, J. P. Doumerc and C. Delmas, *Inorg. Chem.*, 2009, **48**, 7018–7025.
11 R. Berthelot, D. Carlier and C. Delmas, *Nat. Mater.*, 2011, **10**, 74–80.
12 C. Didier, M. Guignard, C. Denage, O. Szajwaj, S. Ito, I. Saadoune, J. Darriet and C. Delmas, *Electrochem. Solid-State Lett.*, 2011, **14**, A75–A78.
13 J. J. Braconnier, C. Delmas and P. Hagenmuller, *Mater. Res. Bull.*, 1982, **17**, 993–1000.
14 A. Mendiboure, C. Delmas and P. Hagenmuller, *J. Solid State Chem.*, 1985, **57**, 323–331.
15 Y. Takeda, K. Nakahara, M. Nishijima, N. Imanishi, O. Yamamoto, M. Takano and R. Kanno, *Mater. Res. Bull.*, 1994, **29**, 659–666.
16 Z. H. Lu and J. R. Dahn, *J. Electrochem. Soc.*, 2001, **148**, A710–A715.
17 Z. H. Lu and J. R. Dahn, *J. Electrochem. Soc.*, 2001, **148**, A1225–A1229.
18 P. Moreau, D. Guyomard, J. Gaubicher and F. Boucher, *Chem. Mater.*, 2010, **22**, 4126–4128.
19 K. T. Lee, T. N. Ramesh, F. Nan, G. Botton and L. F. Nazar, *Chem. Mater.*, 2011, **23**, 3593–3600.
20 B. L. Ellis, T. N. Ramesh, L. J. M. Davis, G. R. Goward and L. F. Nazar, *Chem. Mater.*, 2011, **23**, 5138–5148.
21 R. Tripathi, G. R. Gardiner, M. S. Islam and L. F. Nazar, *Chem. Mater.*, 2011, **23**, 2278–2284.
22 C. Delmas, F. Cherkaoui, A. Nadiri and P. Hagenmuller, *Mater. Res. Bull.*, 1987, **22**, 631–639.
23 C. Delmas, A. Nadiri and J. L. Soubeyroux, *Solid State Ionics*, 1988, **28**, 419–423.
24 J. Gopalakrishnan and K. K. Rangan, *Chem. Mater.*, 1992, **4**, 745–747.
25 D. Kim, S. H. Kang, M. Slater, S. Rood, J. T. Vaughey, N. Karan, M. Balasubramanian and C. S. Johnson, *Adv. Energy Mater.*, 2011, **1**, 333–336.
26 Y. L. Cao, L. F. Xiao, W. Wang, D. W. Choi, Z. M. Nie, J. G. Yu, L. V. Saraf, Z. G. Yang and J. Liu, *Adv. Mater.*, 2011, **23**, 1–6.
27 F. Sauvage, L. Laffont, J. M. Tarascon and E. Baudrin, *Inorg. Chem.*, 2007, **46**, 3289–3294.

28 H. Kim, D. J. Kim, D. H. Seo, M. S. Yeom, K. Kang, D. K. Kim and Y. Jung, *Chem. Mater.*, 2012, **24**, 1205–1211.
29 S.-W. Kim, D.-H. Seo, X. Ma, G. Ceder and K. Kang, *Adv. Energy Mater.*, 2012, **2**, 710–721.
30 H. Kim, D. J. Kim, D.-H. Seo, M. S. Yeom, K. Kang, D. K. Kim and Y. Jung, *Chem. Mater.*, 2012, **24**, 1205–1211.
31 S. P. Ong, V. L. Chevrier, G. Hautier, A. Jain, C. Moore, S. Kim, X. Ma and G. Ceder, *Energy Environ. Sci.*, 2011, **4**, 3680–3688.
32 A. V. d. Ven and G. Ceder, *Phys. Rev. B: Condens. Matter Mater. Phys.*, 1999, **59**, 742–749.
33 A. V. d. Ven, C. Marianetti, D. Morgan and G. Ceder, *Solid State Ionics*, 2000, **135**, 21–32.
34 A. Caballero, L. Hernan, J. Morales, L. Sanchez, J. S. Pena and M. A. G. Aranda, *J. Mater. Chem.*, 2002, **12**, 1142–1147.
35 D. Carlier, J. H. Cheng, R. Berthelot, M. Guignard, M. Yoncheva, R. Stoyanova, B. J. Hwang and C. Delmas, *Dalton Trans.*, 2011, **40**, 9306–9312.
36 Y. Hinuma, Y. S. Meng and G. Ceder, *Phys. Rev. B: Condens. Matter Mater. Phys.*, 2008, **77**, 224111.
37 Y. S. Meng, Y. Hinuma and G. Ceder, *J. Chem. Phys.*, 2008, **128**, 104708.
38 W. W. Pai, S. H. Huang, Y. S. Meng, Y. C. Chao, C. H. Lin, H. L. Liu and F. C. Chou, *Phys. Rev. Lett.*, 2008, **100**, 206404.
39 Y. Hinuma, Y. S. Meng, K. Kang and G. Ceder, *Chem. Mater.*, 2007, **19**, 1790–1800.
40 J. Breger, N. Dupre, P. J. Chupas, P. L. Lee, T. Proffen, J. B. Parise and C. P. Grey, *J. Am. Chem. Soc.*, 2005, **127**, 7529–7537.
41 J. Breger, M. Jiang, N. Dupre, Y. S. Meng, Y. Shao-Horn, G. Ceder and C. P. Grey, *J. Soild State Chem.*, 2005, **178**, 2575–2585.
42 A. Van der Ven and G. Ceder, *Electrochem. Solid–State Lett.*, 2000, **3**, 301–304.
43 K. Kang, Y. S. Meng, J. Breger, C. P. Grey and G. Ceder, *Science*, 2006, **311**, 977–980.
44 E. Markevich, M. D. Levi and D. Aurbach, *J. Electroanal. Chem.*, 2005, **580**, 231–237.
45 S. Yang, X. Wang, X. Yang, Y. Bai, Z. Liu, H. Shu and Q. Wei, *Electrochim. Acta*, 2012, **66**, 88–93.
46 J. Gao and A. Manthiram, *J. Power Sources*, 2009, **191**, 644–647.
47 B. Xu, C. R. Fell, M. Chi and Y. S. Meng, *Energy Environ. Sci.*, 2011, **4**, 2223–2233.
48 C. R. Fell, K. J. Carroll, M. Chi and Y. S. Meng, *J. Electrochem. Soc.*, 2010, **157**, A1202–A1211.
49 J. Rodriguez-Carvajal, *Physica B*, 1993, **192**, 55–69.
50 G. Kresse and D. Joubert, *Phys. Rev. B: Condens. Matter Mater. Phys.*, 1999, **59**, 1758–1775.
51 G. Kresse and J. Furthmuller, *Comput. Mater. Sci.*, 1996, **6**, 15–50.
52 G. Kresse and J. Furthmuller, *Phys. Rev. B: Condens. Matter Mater. Phys.*, 1996, **54**, 11169–11186.
53 G. Kresse, J. Furthmuller and J. Hafner, *Phys. Rev. B: Condens. Matter Mater. Phys.*, 1994, **50**, 13181–13185.
54 J. P. Perdew, K. Burke and Y. Wang, *Phys. Rev. B: Condens. Matter Mater. Phys.*, 1996, **54**, 16533–16539.
55 S. P. Ong, V. L. Chevrier, G. Hautier, A. Jain, C. Moore, S. Kim, X. H. Ma and G. Ceder, *Energy Environ. Sci.*, 2011, **4**, 3680–3688.
56 A. I. Liechtenstein, V. I. Anisimov and J. Zaanen, *Phys. Rev. B: Condens. Matter Mater. Phys.*, 1995, **52**, R5467–R5470.
57 L. Wang, T. Maxisch and G. Ceder, *Phys. Rev. B: Condens. Matter Mater. Phys.*, 2006, **73**, 195107.

